Available online at www.sciencedirect.com
ScienceDirect
Mathematics and Computers in Simulation 202 (2022) 405–420
MATHEMATICS AND COMPUTERS IN SIMULATION
www.elsevier.com/locate/matcom

Original articles

A curvilinear lattice Boltzmann scheme for thermal flows

J.A. Reyes Barraza*, R. Deiterding

School of Engineering, University of Southampton, Boldrewood Campus, SO16 7QF, United Kingdom

Received 2 January 2022; received in revised form 8 May 2022; accepted 3 June 2022
Available online 17 June 2022

Abstract

Lattice Boltzmann schemes are known for their efficiency and low dissipation properties. However, the standard lattice Boltzmann method (LBM) is limited to Cartesian grids, and this approach can be troublesome when approximating thermal flows over curved walls. The present work proposes to solve the two-dimensional lattice Boltzmann equation under curvilinear coordinate transformation to simulate thermal flows with body-fitted grids. Several test cases are discussed, and the results are extensively compared with a very favourable outcome to the available numerical and experimental data, confirming the importance of the implemented methodology. Natural convection in a square cavity and a wavy cavity, as well as flow in a concentric cylindrical annulus are used for validation. Forced convection over a heated two-dimensional cylinder is also included.

Keywords: Convective heat transfer; Curvilinear coordinates; Double-distribution method; Boussinesq approximation

1. Introduction

In recent decades, the lattice Boltzmann method (LBM) has become a valuable and influential development in fluid flow simulations. It is an effective computational method for studying fluid dynamics problems as it is a simple and efficient time-explicit solver that relies only on nearest neighbour communication, making it ideal for massively parallel computations [2]. This method consists of solving a simplified version of the kinetic Boltzmann equation. By a Chapman–Enskog expansion it can be shown that this approach recovers the Navier–Stokes equations [3]. Typically, the LBM employs Cartesian meshes, allowing a straightforward and automatic mesh generation. Hence, the time for setting up simulations, especially for complex geometries, can be reduced considerably. The standard LBM has been shown to be capable of simulating various complex weakly compressible flows [11,14,24], including thermal flows [13,27], which are discussed in this work.

There are many thermal lattice Boltzmann (LB) models available in the literature. The multi-speed approach has been one of the first LB thermal models developed. It is a direct extension of the constant temperature LBM. The advantage of this method is that only one distribution function is needed to obtain the energy evolution. However, the propagation of the particles is not always to the most immediate neighbour, contrary to the widely used isothermal model. Moreover, higher order velocity terms are required in the equilibrium distribution function. The multi-speed models suffer severely from numerical instabilities [28] and are therefore considered impractical for engineering

* Corresponding author.
E-mail address: j.a.reyes@soton.ac.uk (J.A. Reyes Barraza).

https://doi.org/10.1016/j.matcom.2022.06.002

applications. Subsequently, a passive-scalar thermal LB model was introduced by Shan [33]. This approach is based on the assumption that the temperature field can follow the same behaviour as a passive-scalar equation. The passive-scalar approach can be adopted when the viscous heating effects and the compression work done by pressure are negligible. Later, He et al. [17] developed an approach similar to the passive-scalar model, that uses also an independent distribution function to simulate the temperature distribution, but with the advantage that this scheme can incorporate the viscous heat dissipation and the compression work as it simulates the evolution of the internal energy.

Compelling thermal flow simulations are essential in many engineering applications [20,21]. Convection driven by temperature differences in enclosed spaces is particularly important [25,31]. In many practical problems, it is crucial to know the thermal effects simultaneously with the fluid motion. Typical applications include cooling and heating systems, for instance, for solar collector receivers, radiators, electronics and nuclear reactors [30]. Some of these simulations require the treatment of curved boundary conditions for which Cartesian grids are not ideal. Note also that thermal flows can involve crucially important thermal boundary layers that can be resolved more effectively with non-uniform grids.

One effort to treat curved boundaries in thermal flows with Cartesian LBM effectively, but with non-uniform meshes, has been proposed done by Feldhusen et al. [13], using the AMROC-LBM solver. This advanced LBM Cartesian solver employs block-structured adaptive mesh refinement [10], which is significantly more effective than using the predominantly isotropic refinement of individual cells [4]. In addition, they have included an algorithm for complex geometry wall boundary conditions for numerical simulations with moving structures. Kuznik et al. [26] implemented a Taylor series expansion and least-square-based Lattice Boltzmann method (TLLBM), which allows LBM simulations with non-uniform grids, showing the computational benefits of a non-uniform grid for a thermal LBM. Also, Wang et al. [38] developed a thermal lattice Boltzmann flux solver for simulations of natural and mixed convection with the body-fitted strategy for meshing curved boundary conditions.

In here, the generalised LBM developed in [32] is extended to thermal flows simulations with the body-fitted strategy for meshing. The passive-scalar model with double-distribution from Shan [33] is employed for the temperature evolution. The resulting scheme is hence appropriate when the viscous heat dissipation and the compression work are insignificant. The organisation of this paper is as follows: The LB thermal model is presented in Section 2, as well as the extension to curvilinear coordinates. In Section 3, three 2D test cases are presented, including natural convection in the square cavity and a wavy cavity, thermal flow in a concentric cylindrical annulus, and the last test case conducted is forced convection over a heated two-dimensional cylinder. The conclusions can be found in Section 4.

2. Methodology

2.1. Thermal lattice Boltzmann

In this work, the well-known kinetic model with single relaxation-time and the Bhatnagar–Gross–Krook (BGK) approximation in two dimensions (D2Q9) is employed. Therefore, the discrete-velocity Boltzmann equation with an external force can be written as

$$\frac{\partial f_\alpha}{\partial t} + \mathbf{e}_\alpha \cdot \nabla f_\alpha = -\frac{1}{\tau_\nu}\left(f_\alpha - f_\alpha^{eq}\right) + F_\alpha, \tag{1}$$

where f_α ($\alpha = 0, 1..., 8$) is the particle distribution function, $\mathbf{e}_\alpha$ is the particle velocity, τ_ν the relaxation time, f_α^{eq} is the equilibrium distribution function and F_α is the external force.

The evolution of the second set of distribution functions for the D2Q9 model can be written as

$$\frac{\partial g_\alpha}{\partial t} + \mathbf{e}_\alpha \cdot \nabla g_\alpha = -\frac{1}{\tau_T}\left(g_\alpha - g_\alpha^{eq}\right), \tag{2}$$

where g_α ($\alpha = 0, 1..., 8$) is the temperature distribution function, g_α^{eq} is the corresponding equilibrium distribution for the temperature field and τ_T is the thermal relaxation time.

In the D2Q9 model, the lattice velocities $\mathbf{e}_\alpha$ can be written as

$$\mathbf{e}_\alpha = \begin{cases} (0,0)c & \alpha = 0 \\ (\pm 1, 0)c, (0, \pm 1)c & \alpha = 1, 2, 3, 4 \\ (\pm 1, \pm 1)c, (\mp 1, \pm 1)c & \alpha = 5, 6, 7, 8 \end{cases}, \tag{3}$$

with $c = \delta x/\delta t$; δx denotes the lattice speed and δt is the time step [39]. In this work, $c = 1$.

A Maxwell distribution up to second-order terms is used as equilibrium distribution function, i.e.,

$$f_\alpha^{eq} = w_\alpha \rho(x,t)\left[1 + \frac{\mathbf{e}_\alpha \mathbf{u}}{c_s^2} + \frac{(\mathbf{e}_\alpha \mathbf{u})^2}{2c_s^4} - \frac{\mathbf{u}^2}{2c_s^2}\right], \tag{4}$$

with coefficients w_α ($w_0 = 4/9$, $w_{1,2,3,4} = 1/9$ and $w_{5,6,7,8} = 1/36$). c_s is the speed of sound, which is calculated as $c_s = c/\sqrt{3}$, and the vector $\mathbf{u} = (u, v)$ denotes the macroscopic velocities.

The equilibrium distribution function for the temperature field reads

$$g_\alpha^{eq} = w_\alpha T(x,t)\left[1 + \frac{\mathbf{e}_\alpha \mathbf{u}}{c_s^2}\right]. \tag{5}$$

Since the fluid is approximated to be incompressible, a linear dependency between temperature differences and gravitational forces can be applied, which is known as the Boussinesq approximation [29]. F_α can be expressed as

$$F_\alpha = \frac{w_\alpha \mathbf{F} \cdot \mathbf{e}_\alpha}{c_s^2}, \tag{6}$$

with

$$\mathbf{F} = \mathbf{g}\beta(T - T_{\text{ref}}), \tag{7}$$

where $\mathbf{g}$ is the acceleration vector of gravity and β is the coefficient of thermal expansion. T and T_{ref} are the temperature and the reference temperature, respectively. The force term establishes the coupling between the momentum equation with the temperature transport equation for natural convection.

It can be demonstrated through the Chapman–Enskog analysis that the presented method recovers the Navier–Stokes equations near the incompressible limit [15], i.e.

$$\frac{\partial \rho}{\partial t} + \nabla \cdot (\rho \mathbf{u}) = 0, \tag{8}$$

$$\frac{\partial \mathbf{u}}{\partial t} + \mathbf{u} \cdot \nabla \mathbf{u} = -\frac{\nabla p}{\rho} + \nu \nabla^2 \mathbf{u} + \mathbf{F}. \tag{9}$$

After disregarding the viscous heat dissipation and the compression work, the temperature field satisfies a passive-scalar equation, i.e.

$$\frac{\partial T}{\partial t} + \mathbf{u} \cdot \nabla T = \chi \nabla^2 T. \tag{10}$$

The kinematic viscosity ν and the relaxation time are related by the relation

$$\nu = c_s^2 \left(\tau_\nu - \frac{\Delta t}{2}\right), \tag{11}$$

which becomes imminent throughout the Chapman–Enskog analysis. Similarly, the relation between the thermal diffusivity coefficient χ and the relaxation time τ_T reads

$$\chi = c_s^2 \left(\tau_T - \frac{\Delta t}{2}\right). \tag{12}$$

The macroscopic quantities such as density, velocity, temperature and pressure can be evaluated by

$$\rho = \sum f_\alpha, \quad \mathbf{u} = \frac{1}{\rho} \sum f_\alpha \boldsymbol{e}_\alpha, \quad T = \sum g_\alpha, \quad p = \rho c_s^2. \tag{13}$$

2.2. Curvilinear coordinate transformation

The idea of the generalised curvilinear coordinate system is to transform a curvilinear grid in physical space in terms of x and y to an equally spaced computational grid in terms of ξ and η. Therefore, the independent variables (x, y) in Eqs. (1) and (2) are transformed to the new coordinates (ξ, η) as

$$\xi = \xi(x, y), \quad \eta = \eta(x, y). \tag{14}$$

The chain rule of partial derivatives is applied to transform the physical space into the computational space, i.e.,

$$\frac{\partial}{\partial x} = \frac{\partial}{\partial \xi}\frac{\partial \xi}{\partial x} + \frac{\partial}{\partial \eta}\frac{\partial \eta}{\partial x}, \quad \frac{\partial}{\partial y} = \frac{\partial}{\partial \xi}\frac{\partial \xi}{\partial y} + \frac{\partial}{\partial \eta}\frac{\partial \eta}{\partial y}. \tag{15}$$

The curvilinear grid in the physical space is connected to the rectangular grid in the computational space by

$$\begin{bmatrix} \xi_x & \xi_y \\ \eta_x & \eta_y \end{bmatrix} = \frac{1}{J}\begin{bmatrix} y_\eta & -x_\eta \\ -y_\xi & x_\xi \end{bmatrix}, \tag{16}$$

where the Jacobian J of the transformation becomes

$$J = x_\xi y_\eta - x_\eta y_\xi. \tag{17}$$

Using Eq. (15), one can expresses the convection term of Eq. (1) as

$$\begin{aligned} \mathbf{e}_\alpha \cdot \nabla f_\alpha &= e_{\alpha x}\frac{\partial f_\alpha}{\partial x} + e_{\alpha y}\frac{\partial f_\alpha}{\partial y} = e_{\alpha x}\left(\frac{\partial f_\alpha}{\partial \xi}\frac{\partial \xi}{\partial x} + \frac{\partial f_\alpha}{\partial \eta}\frac{\partial \eta}{\partial x}\right) + e_{\alpha y}\left(\frac{\partial f_\alpha}{\partial \xi}\frac{\partial \xi}{\partial y} + \frac{\partial f_\alpha}{\partial \eta}\frac{\partial \eta}{\partial y}\right) \\ &= \left(e_{\alpha x}\frac{\partial \xi}{\partial x} + e_{\alpha y}\frac{\partial \xi}{\partial y}\right)\frac{\partial f_\alpha}{\partial \xi} + \left(e_{\alpha x}\frac{\partial \eta}{\partial x} + e_{\alpha y}\frac{\partial \eta}{\partial y}\right)\frac{\partial f_\alpha}{\partial \eta} = \tilde{e}_{\alpha\xi}\frac{\partial f_\alpha}{\partial \xi} + \tilde{e}_{\alpha\eta}\frac{\partial f_\alpha}{\partial \eta}, \end{aligned} \tag{18}$$

where

$$\tilde{\mathbf{e}}_\alpha = (\tilde{e}_{\alpha\xi}, \tilde{e}_{\alpha\eta}) = (e_{\alpha x}\xi_x + e_{\alpha y}\xi_y, e_{\alpha x}\eta_x + e_{\alpha y}\eta_y). \tag{19}$$

Hence, the single-relaxation-time lattice Boltzmann equation in the computational space can be written as

$$\frac{\partial f}{\partial t} + \tilde{e}_{\alpha\xi}\frac{\partial f_\alpha}{\partial \xi} + \tilde{e}_{\alpha\eta}\frac{\partial f_\alpha}{\partial \eta} = -\frac{1}{\tau_v}\left(f_\alpha - f_\alpha^{eq}\right) + F_\alpha. \tag{20}$$

If one applies the same procedure to the convective terms in Eq. (2), one obtains

$$\frac{\partial g}{\partial t} + \tilde{e}_{\alpha\xi}\frac{\partial g_\alpha}{\partial \xi} + \tilde{e}_{\alpha\eta}\frac{\partial g_\alpha}{\partial \eta} = -\frac{1}{\tau_T}\left(g_\alpha - g_\alpha^{eq}\right). \tag{21}$$

2.3. Numerical scheme

Eqs. (20) and (21) are solved similarly to the streaming-collision procedure commonly used in the LBM. The streaming step advects the density distribution functions and in the collision step they are relaxed toward equilibrium. For clarity, the convection terms in Eq. (20) are grouped as

$$A_\alpha = \tilde{e}_{\alpha\xi}\frac{\partial f_\alpha}{\partial \xi} + \tilde{e}_{\alpha\eta}\frac{\partial f_\alpha}{\partial \eta}, \tag{22}$$

Second-order-accurate central finite-differences are used to discretise the spatial derivatives as

$$\left.\frac{\partial f_\alpha}{\partial \xi}\right|_{(i,j)} = \frac{f_{\alpha_{(i+1,j)}} - f_{\alpha_{(i-1,j)}}}{2\Delta\xi}, \tag{23}$$

$$\left.\frac{\partial f_\alpha}{\partial \eta}\right|_{(i,j)} = \frac{f_{\alpha_{(i,j+1)}} - f_{\alpha_{(i,j-1)}}}{2\Delta\eta}. \tag{24}$$

The indices i and j denote the ξ and η directions, respectively. For temporal advancement, an explicit fourth-order Runge–Kutta method is applied:

$$f_\alpha^1 = f_\alpha^t, \quad f_\alpha^2 = f_\alpha^1 - \frac{\Delta t}{4}A_\alpha^1, \quad f_\alpha^3 = f_\alpha^1 - \frac{\Delta t}{3}A_\alpha^2, \quad f_\alpha^4 = f_\alpha^1 - \frac{\Delta t}{2}A_\alpha^3, \quad f_\alpha^* = f_\alpha^1 - \Delta t A_\alpha^4, \tag{25}$$

where the superscripts 1, 2, 3, and 4 are used to indicate the time level at each Runge–Kutta stage.

When non-linearities are present, central differencing of convective terms can become unstable [19]. Therefore, it is necessary to add a damping term to stabilise the solution. In this work, a fourth-order dissipation term is added, and it is defined as

$$D_e = -\epsilon_e\left((\Delta\xi)^4\frac{\partial^4 f_\alpha}{\partial \xi^4} + (\Delta\eta)^4\frac{\partial^4 f_\alpha}{\partial \eta^4}\right), \tag{26}$$

with ϵ_e being a tunable coefficient. Fourth-order central differences are applied to approximate the derivatives in Eq. (26) as

$$\begin{aligned}(\Delta\xi)^4 \frac{\partial^4 f_\alpha}{\partial \xi^4}\bigg|_{(i,j)} &= f_{\alpha_{(i-2,j)}} - 4f_{\alpha_{(i-1,j)}} + 6f_{\alpha_{(i,j)}} - 4f_{\alpha_{(i+1,j)}} + f_{\alpha_{(i+2,j)}},\\ (\Delta\eta)^4 \frac{\partial^4 f_\alpha}{\partial \eta^4}\bigg|_{(i,j)} &= f_{\alpha_{(i,j-2)}} - 4f_{\alpha_{(i,j-1)}} + 6f_{\alpha_{(i,j)}} - 4f_{\alpha_{(i,j+1)}} + f_{\alpha_{(i,j+2)}}.\end{aligned} \tag{27}$$

The dissipation term is subsequently added directly, as described by Hoffmann et al. [19], i.e.

$$f_\alpha^{**} = f_\alpha^{*} + D_e. \tag{28}$$

To complete the method, the collision step is performed as

$$f_\alpha^{t+\Delta t} = f_\alpha^{**} - \frac{\Delta t}{\tau_v}\left(f_\alpha^{**} - f_\alpha^{eq**}\right) + \Delta t F_\alpha. \tag{29}$$

After updating the particle velocity distribution function, the same procedure is applied for the temperature distributions g_α.

There are two predominant types of boundary conditions, Dirichlet and Neumann. For the Dirichlet boundary condition, the variables are fixed to a specific value. For the Neumann boundary condition, a derivative is assigned to the boundary that is generally calculated using finite differences. For instance, at the wall boundary a non-split condition is applied, i.e. the macroscopic velocities are set to zero ($u, v = 0$) and also the pressure gradient at the wall-normal direction ($\partial p/\partial y_n = 0$) is prescribed, which can be approximated with second-order-accurate extrapolation.

In the LBM, boundary conditions are implemented differently than for conventional fluid dynamics solvers. The approach requires boundary conditions in terms of particle distribution functions, which necessitates a special treatment to calculate their values based on the macroscopic variables at each boundary. In this work, the distribution functions are determined by implementing the ideas of Guo et al. [16], where the non-equilibrium part is obtained by extrapolation. Therefore, here the distribution functions are calculated by

$$f_\alpha = f_\alpha^{eq} + f_\alpha^{non\text{-}eq}, \tag{30}$$

where f_α^{eq} is obtained by calling the equilibrium function and $f_\alpha^{non\text{-}eq}$ by extrapolating the interior values.

3. Numerical results

Several numerical simulations are conducted to verify the proposed scheme and quantify its performance. These include natural convection within different geometries, such as a square cavity, a wavy cavity, and a concentric cylindrical annulus. Moreover, simulations of forced convection in external flow around a heated circular cylinder are also included. All the results are compared with available validation data by others.

In thermal flows, there are several critical non-dimensional parameters such as the Prandtl number

$$\mathrm{Pr} = \frac{\nu}{\chi}, \tag{31}$$

the local Nusselt number at the wall

$$\mathrm{Nu} = \frac{L_c}{\Delta T}\left(\frac{\partial T}{\partial \eta}\right)_{wall}, \tag{32}$$

and the Rayleigh number, defined as

$$\mathrm{Ra} = \frac{\mathbf{g}\beta\Delta T L_c^3}{\nu\chi}, \tag{33}$$

where L_c is the characteristic length, which is typically the geometry height; ΔT is the temperature difference between hot T_h and cold T_c boundaries. The characteristic thermal velocity is defined as $U = \sqrt{\mathbf{g}\beta\Delta T L_c}$.

For the following simulations, $\mathrm{Pr} = 0.71$, U is close to 0.1 and $\epsilon_e = 0.001$. For convenience, the parameters chosen to solve the governing equations are $\Delta\xi = 1$, $\Delta\eta = 1$ and Δt varies depending on the grid. The value of T_{ref} in Eq. (7) is the same as the cold boundary ($T_c = 0$) and this is also the initial temperature for the entire fluid field, except for the hot wall boundary ($T_h = 0$). The numerical simulations are carried out in lattice units, i.e. all internal variables are non-dimensional.

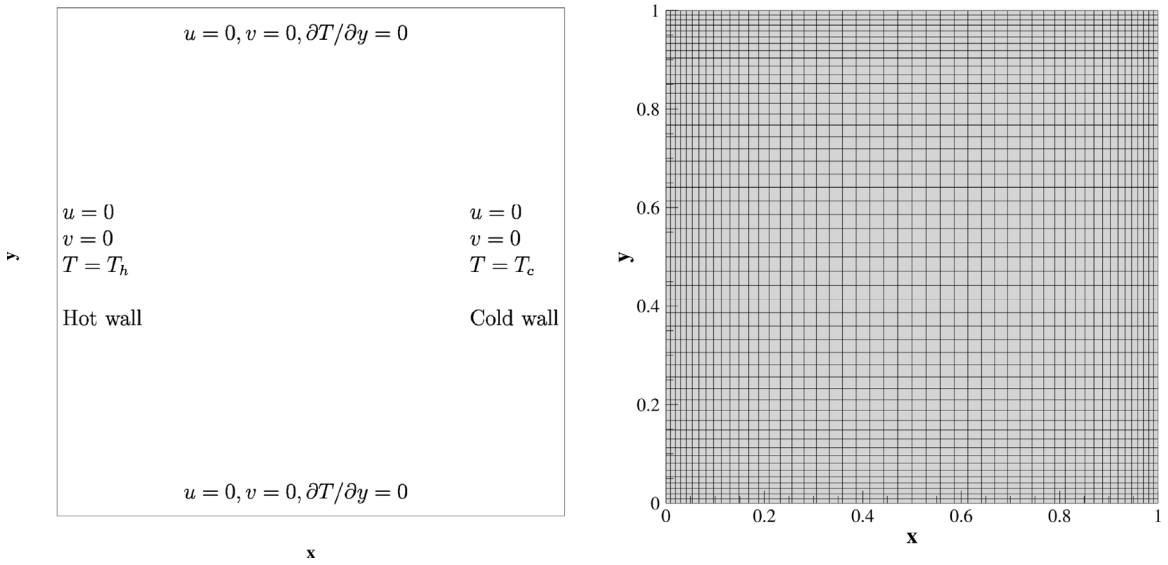

Fig. 1. Boundary conditions and stretched mesh used for the natural convection in the square cavity.

3.1. Natural convection in the 2D square cavity and a wavy cavity

Natural convection in a square cavity is a classical benchmark where the temperature difference drives the flow inside the cavity. This test case consists of having two walls with constant but different temperatures T_h and T_c, and the rest of the walls need to have adiabatic boundary conditions. At all four domain boundaries, no-slip wall boundary conditions are prescribed. Fig. 1 shows the thermal and momentum boundary conditions that apply in this test case. The wavy cavity has the same setup.

The square cavity convection problem has been solved with a stretched grid (cf. Fig. 1) to demonstrate that the present method can resolve the classical benchmark test with non-Cartesian grids. The mesh can be stretched by applying the transformation

$$\begin{aligned} x &= H\frac{(2\alpha+\lambda)[(\lambda+1)/(\lambda-1)]^{(\xi-\alpha)/(1-\alpha)}+2\alpha-\lambda}{(2\alpha+1)\left(1+[(\lambda+1)/(\lambda-1)]^{(\xi-\alpha)/(1-\alpha)}\right)}, \\ y &= H\frac{(2\alpha+\lambda)[(\lambda+1)/(\lambda-1)]^{(\eta-\alpha)/(1-\alpha)}+2\alpha-\lambda}{(2\alpha+1)\left(1+[(\lambda+1)/(\lambda-1)]^{(\eta-\alpha)/(1-\alpha)}\right)}, \end{aligned} \tag{34}$$

where λ determines the level of the stretching, α defines how the mesh nodes are distributed, and H is the length. If $\alpha = 0.5$, the mesh elements in the centre will be enlarged uniformly; therefore, the grid will cluster towards the edges of the cavity. If $\alpha = 0$, the clustering will take place at H. In this work, all simulations have used $\alpha = 0.5$ and $\lambda = 1.2$. The wavy cavity has a deformed mesh and the same aspect ratio as the square cavity. To obtain the grid for the wavy cavity, it is necessary to apply the mapping

$$x = \xi + \mu\sin(4\pi\eta), \quad y = \eta + \mu\sin(4\pi\xi), \tag{35}$$

where μ determines the amount of grid deformation. Here $\mu = 0.025$ is used.

For the following simulations, four different Rayleigh numbers were selected: $\mathrm{Ra} = 10^3$, 10^4, 10^5 and 10^6. For the square cavity, two mesh resolutions were selected: (101×101) for the lowest Rayleigh number ($\mathrm{Ra} = 10^3$), and (201×201) for the rest of the simulations. For the wavy cavity, different mesh resolutions are utilised, and these are specified in Table 2. At these values of Ra, the solution converges to a steady-state condition after sufficient simulation time. The results shown have been extracted when the changes in the average Nusselt number are negligible.

The results of the 2D squared cavity are presented and compared with the available literature in Table 1. This table includes the Navier–Stokes solutions from De Vahl Davis [9], who solved them on a uniform mesh with a

Table 1
Natural convection in the square at different Rayleigh numbers.

Ra	Author(s)	u_{max}	y_{max}	v_{max}	x_{max}	$\overline{\mathrm{Nu}}$
10^3	De Vahl Davis [9]	3.649	0.813	3.697	0.178	1.114
	Feldhusen et al. [13]	3.640	0.810	3.688	0.180	1.115
	Wang et al. [38]	3.640	0.815	3.708	0.180	1.115
	D'Orazio et al. [12]	3.653	0.812	3.701	0.179	1.117
	Present	3.654	0.812	3.720	0.178	1.104
10^4	De Vahl Davis [9]	16.178	0.823	19.617	0.119	2.245
	Feldhusen et al. [13]	16.161	0.823	19.595	0.118	2.239
	Wang et al. [38]	16.140	0.825	19.670	0.118	2.232
	D'Orazio et al. [12]	16.237	0.820	19.680	0.117	2.235
	Present	16.287	0.822	19.800	0.117	2.243
10^5	De Vahl Davis [9]	34.730	0.855	68.590	0.066	4.510
	Feldhusen et al. [13]	34.666	0.855	68.457	0.066	4.504
	Wang et al. [38]	34.870	0.855	68.850	0.065	4.491
	D'Orazio et al. [12]	34.822	0.852	68.712	0.063	4.504
	Present	35.576	0.856	69.241	0.064	4.410
10^6	De Vahl Davis [9]	64.630	0.850	219.360	0.038	8.806
	Feldhusen et al. [13]	64.756	0.850	220.125	0.038	8.804
	Wang et al. [38]	64.838	0.850	220.920	0.038	8.711
	D'Orazio et al. [12]	64.868	0.852	221.187	0.039	8.767
	Present	67.027	0.852	227.712	0.035	8.679

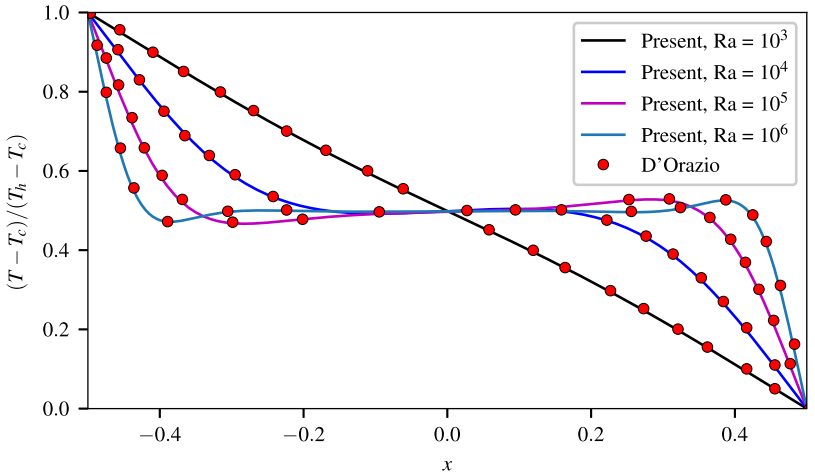

Fig. 2. Temperature profiles at the mid-height of the square cavity.

second-order finite-difference method, the results obtained by Feldhusen et al. [13] using an incompressible thermal LBM with block-structured mesh refinement (AMROC-LBM), the solutions of the thermal lattice Boltzmann flux solver from Wang et al. [38], and the results of a thermal lattice BGK model with doubled populations from D'Orazio et al. [12]. Fig. 2 compares the normalised temperature profile obtained with the present methodology at the mid-height of the squared cavity with the results obtained by D'Orazio et al. [12], and it shows a good agreement for all Rayleigh numbers.

The variables shown in Table 1 are the maximal horizontal velocity component u_{max} at the mid-width of the cavity, the location y_{max} of the maximal horizontal velocity, the maximal vertical velocity component at the mid-height of the cavity v_{max}, the location x_{max} of its occurrence and the average Nusselt number $\overline{\mathrm{Nu}}$ at the hot wall of the cavity. u_{max} and v_{max} are normalised by χ/H, where H is the height of the cavity. The average Nusselt number

Table 2
Natural convection in a wavy cavity at different Rayleigh numbers.

Ra	Grid resolution ($N \times N$)	u_{max}	y_{max}	v_{max}	x_{max}	$\overline{\mathrm{Nu}}$
10^3	(201 × 201)	3.491	0.810	3.553	0.180	1.175
10^4	(201 × 201)	15.914	0.815	19.153	0.115	2.318
	(401 × 401)	15.897	0.813	19.140	0.118	2.331
10^5	(201 × 201)	34.338	0.840	68.831	0.060	4.611
	(401 × 401)	33.852	0.840	67.424	0.063	4.513
10^6	(401 × 401)	67.631	0.830	239.743	0.030	9.559

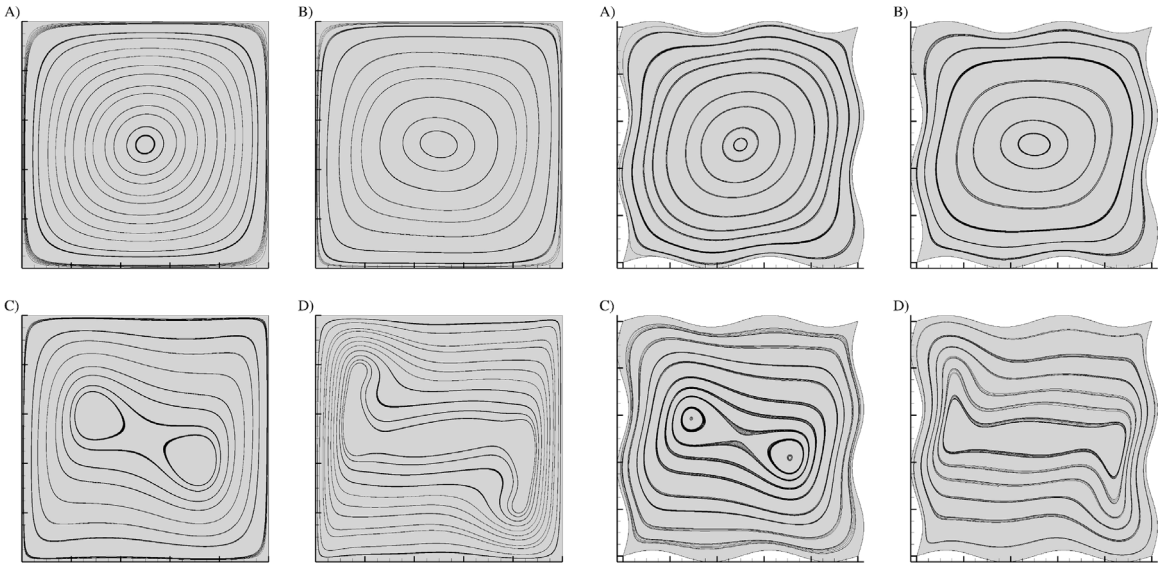

Fig. 3. Streamlines of natural convection in the square cavity and a wavy cavity at different Rayleigh numbers: (A) Ra = 10^3, (B) Ra = 10^4, (C) Ra = 10^5 and (D) Ra = 10^6.

is obtained by integrating the local Nusselt number (Nu) defined in Eq. (32) on the hot surface as

$$\overline{\mathrm{Nu}} = -\frac{1}{L_s}\int_0^{L_s} \mathrm{Nu}\, ds. \tag{36}$$

The integration in Eq. (36) is simply the summation of the local Nu data on the surface divided by the length of the same surface. Therefore, for the square cavity $L_s = H$, but this is not necessarily the case for the wavy cavity, since it has larger surface and thereby increased length. Nevertheless, as characteristic length of the wavy cavity also the height H has been used in order to have the same driven force characterised by Ra. It can be seen in Table 1 that u_{max}, v_{max} and the $\overline{\mathrm{Nu}}$ increase as the Rayleigh number increases, as it is expected. In general, the proposed scheme exhibits good agreement with previously published validation results.

Table 2 shows the results obtained for natural convention at different Rayleigh numbers in a wavy cavity for different grid resolutions, where N is the number of nodes. When comparing the results of the square cavity against the wavy cavity, minor differences are found between them, so the solutions generally agree with each other. Although many authors have solved natural convection in wavy cavities using traditional numerical methods [1,6,23], a direct comparison for the exact cavity used in this section is not available in the literature. Still, the methodology implemented can handle curved wall boundary conditions apparently well and presented predictions appear plausible. The streamlines show the flow field for the two types of cavities in Fig. 3 for all Ra numbers.

Fig. 4 shows the error convergence analysis for the average Nusselt number error ($\varepsilon\overline{\mathrm{Nu}}$) at Ra = 10^4. This analysis was performed on Cartesian grids and with four different mesh resolutions (N = 21, 31, 41 and 51). In addition to the order of accuracy analysis, a global mass conservation analysis has been conducted considering the average

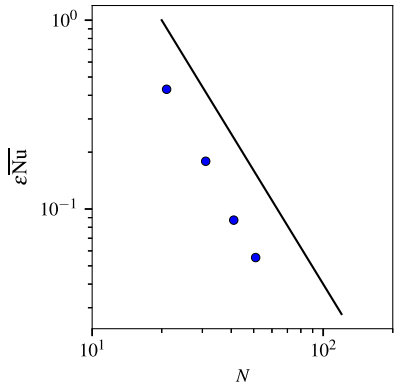

Fig. 4. Error convergence analysis for natural convection in the 2D square cavity at $\mathrm{Ra} = 10^4$.

Table 3
Mass conservation analysis for natural convection in the 2D square cavity at $\mathrm{Ra} = 10^3$.

t^*	Uniform grid		Stretched grid	
	$\overline{\rho}/\rho_0$	$\overline{\mathrm{Nu}}$	$\overline{\rho}/\rho_0$	$\overline{\mathrm{Nu}}$
5	1.0000	1.406	0.9999	1.408
10	0.9999	1.145	0.9998	1.149
15	0.9998	1.106	0.9996	1.110
20	0.9996	1.101	0.9995	1.105
25	0.9995	1.100	0.9993	1.104

density $\overline{\rho}$ of the entire field and the initial density value ρ_0. Since this numerical scheme implements boundary conditions at nodal locations, global mass conservation cannot be expected. For a numerical mass conservation assessment, numerical simulations at $\mathrm{Ra} = 10^3$ on two different grids (one uniform and one stretched) with the same resolution ($N = 101$) were performed. Table 3 shows the density ratio $\overline{\rho}/\rho_0$ at different dimensionless time $t^* = tU/L_c$ and the Nusselt number to show convergence. The implemented numerical scheme approximates the theoretically expected second-order accuracy and the mass losses are negligible, albeit increasing with the number of time steps, as expected.

3.2. Natural convection in a concentric cylindrical annulus

Multiple investigations have been carried out to study the flow driven by temperature differences in concentric cylindrical annuli [8,25]. However, most of the studies of natural convection using the Cartesian LBM deal with square enclosures [22,34,37]. Nonetheless, some authors have used non-Cartesian LBM for this problem [5,27,38]. Therefore, this configuration is a valuable benchmark in the context of this work, so several numerical simulations of thermal flow in a concentric annulus over a wide range of Rayleigh numbers are performed.

This test case consists of natural convection within a circular enclosure made of two circles with the same centre. The flow within this geometry is driven by the temperature difference of a cold outer circular wall with constant temperature and an inner circular wall at a larger temperature. Fig. 5 shows the schematic diagram for natural convection in a concentric annulus. The non-dimensional wall temperature of the inner cylinder with a radius of R_i is set to $T_i = 1.0$, and the wall temperature of the outer cylinder with a radius of R_0 is $T_0 = 0.0$. No-slip boundary conditions are applied on the inner and outer cylinders. The distance between these two cylinders is the characteristic length for this test case. The aspect ratio of the problem is defined as

$$\mathrm{Ar} = \frac{R_0}{R_i}. \tag{37}$$

In this work, the aspect ratio is $\mathrm{Ar} = 2.6$. Four different Rayleigh numbers ($\mathrm{Ra} = 10^2, 10^3, 10^4$ and 5×10^5) are selected to carry out the simulations. A simple O-type grid with body-fitted boundary conditions and without

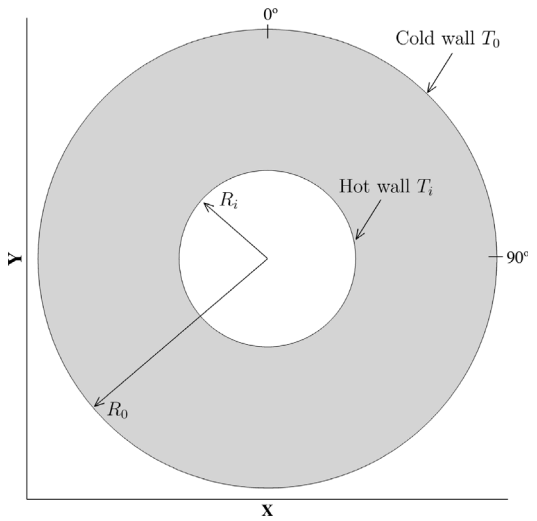

Fig. 5. Boundary conditions and domain configuration of natural convection in a concentric cylindrical annulus diagram.

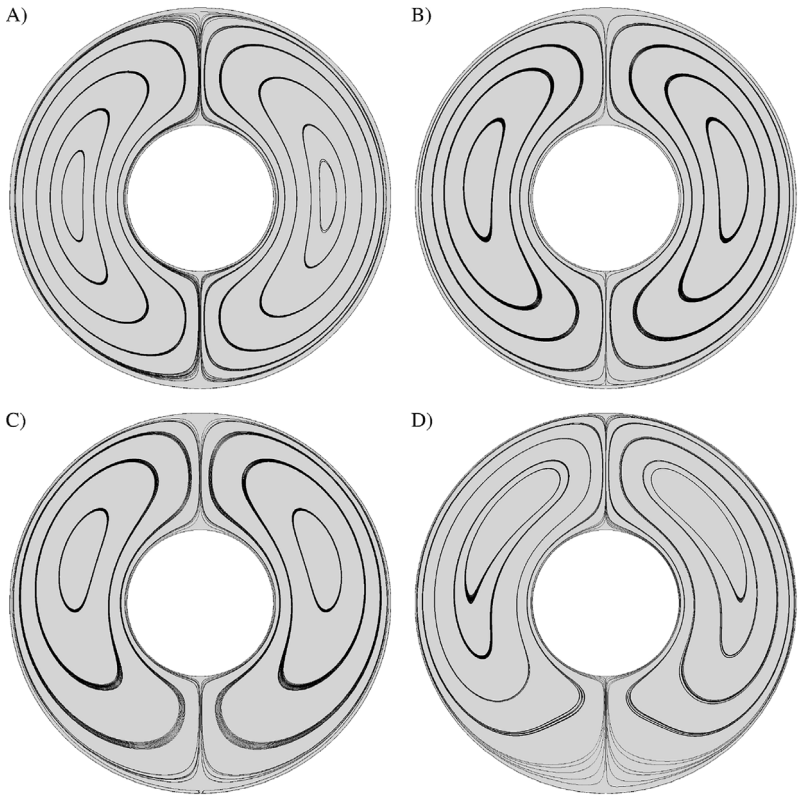

Fig. 6. Flow field shown by streamlines of natural convection in a concentric cylindrical annulus: (A) $\mathrm{Ra} = 10^2$, (B) $\mathrm{Ra} = 10^3$, (C) $\mathrm{Ra} = 10^4$ and (D) $\mathrm{Ra} = 5 \times 10^4$.

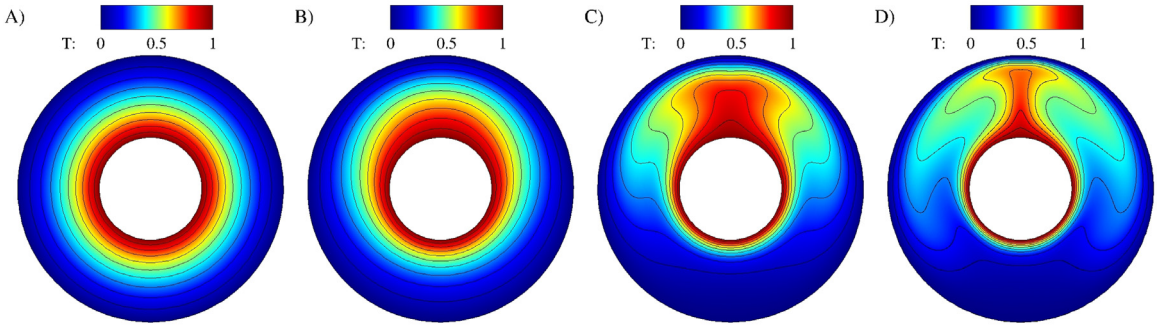

Fig. 7. Flow field shown by the temperature field of natural convection in a concentric cylindrical annulus: (A) $\mathrm{Ra} = 10^2$, (B) $\mathrm{Ra} = 10^3$, (C) $\mathrm{Ra} = 10^4$ and (D) $\mathrm{Ra} = 5 \times 10^4$.

any stretching is used. Three different grid resolutions were used for the simulations (257×257) for the lowest Rayleigh numbers ($\mathrm{Ra} = 10^2$ and $\mathrm{Ra} = 10^3$), (769×769) for the highest, and (513×513) for the remaining. The average equivalent heat conductivity for the inner $\left(\overline{K_{eq_i}}\right)$ and outer $\left(\overline{K_{eq_0}}\right)$ cylinder can be calculated by

$$\overline{K_{eq_i}} = \frac{R_i \ln(\mathrm{Ar})}{(T_i - T_0)} \frac{1}{2\pi} \int_0^{2\pi} \frac{\partial T}{\partial \eta} d\theta, \tag{38}$$

$$\overline{K_{eq_0}} = \frac{R_0 \ln(\mathrm{Ar})}{(T_i - T_0)} \frac{1}{2\pi} \int_0^{2\pi} \frac{\partial T}{\partial \eta} d\theta. \tag{39}$$

Fig. 6 shows the streamlines of the concentric cylindrical annulus at different Rayleigh numbers. When the fluid is enclosed in the annulus and under the influence of forces derived by the temperature differences, it will generate vortices. At small Rayleigh number, i.e. $\mathrm{Ra} = 10^2$, the driving force is small and the fluid moves weakly. At this condition, the centre of the vortex is almost located in the middle of the annulus, as it can be seen in Fig. 6A. When the Rayleigh number is increased, the centre of the vortices move up gradually. Fig. 7 shows the temperature distribution at different Rayleigh numbers. It can be seen that the temperature levels are concentric to the cylinders at low $\mathrm{Ra} = 10^2$, but as the Rayleigh number increases, the temperature distribution becomes partially eccentric; then the temperature fields take different shapes at the highest Rayleigh numbers, i.e. $\mathrm{Ra} = \times 10^4$ and $\mathrm{Ra} = 5 \times 10^4$.

Table 4 compares the average equivalent heat conductivities of the inner and outer cylinders quantitatively at various Rayleigh numbers. The results of Kuehn and Goldstein [25], Wang et al. [38] and Shu [36] are included. Kuehn and Goldstein [25] have presented a quite comprehensive study. They have not only conducted numerical simulation, but they have also validated their solver with experimental data, making the study of great value. The reference data points in this work have been extracted from that paper. On the other hand, Wang et al. [38] considered the results from Shu [36] as reference because they have used a high-order numerical method. Additionally, dimensionless temperature profiles at different radial positions, namely $\theta = 0°$, $\theta = 30°$ and $\theta = 90°$ have been compared with the numerical results of Kuehn and Goldstein [25]. Fig. 8 exhibits an excellent agreement between the proposed methodology and the mentioned study. The results presented here demonstrate the capability of the present method to solve heat transfer problems with curved boundaries.

3.3. Heated two-dimensional circular cylinder

Unlike natural convection that happens inherently due to the temperature difference of the fluid, forced convection is a heat transfer process that happens by an external source. This test case is used here to verify and validate that our proposal can correctly handle curved temperature boundaries along with velocity-inlet and pressure-outlet boundary conditions. In order to do this, our simulations are compared with the literature available for forced convection. In forced convection, the energy equation, Eq. (10), is solved after obtaining the flow field. Here, the momentum and energy equations are not coupled through a force, thereby $\mathbf{F} = 0$ in Eq. (1).

In this section, only steady-state simulations are carried out at three different Reynolds numbers: $\mathrm{Re} = 10$, 20 and 40. An O-grid type with two different grid resolutions are used for each Reynolds number (129×129)

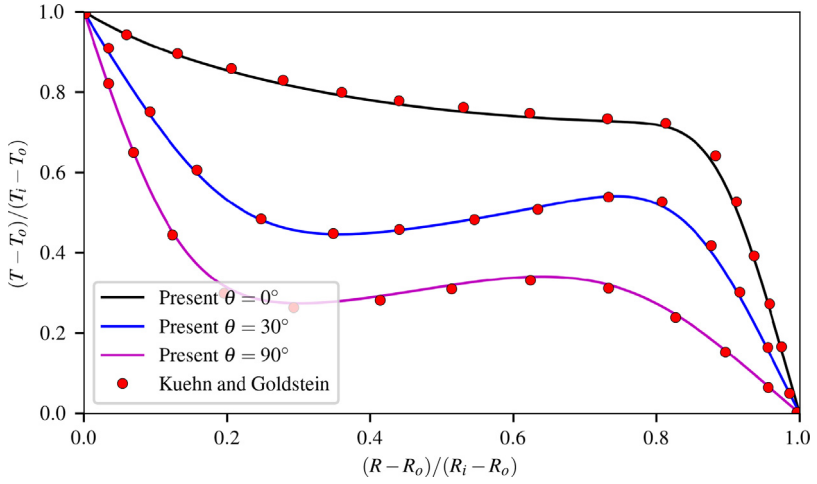

Fig. 8. Temperature profiles at different azimuthal positions for natural convection in a concentric cylindrical annulus at $\mathrm{Ra} = 5 \times 10^4$.

Table 4
Natural convection in a concentric cylindrical annulus at different Rayleigh numbers.

	Author(s)	Rayleigh number			
		10^2	10^3	10^4	5×10^4
Inner ring	Kuehn and Goldstein [25]	1.000	1.081	2.010	3.024
	Wang et al. [38]	1.002	1.076	1.960	2.941
	Shu [36]	1.001	1.082	1.979	2.958
	Present	0.992	1.071	1.972	2.916
Outer ring	Kuehn and Goldstein [25]	1.002	1.084	2.005	2.973
	Wang et al. [38]	1.002	1.078	1.960	2.941
	Shu [36]	1.001	1.082	1.979	2.958
	Present	0.994	1.073	1.973	2.917

Table 5
Steady flow with forced convection over a circular cylinder at different Reynolds numbers.

Author(s)	$\overline{\mathrm{Nu}}$		
	$\mathrm{Re} = 10$	$\mathrm{Re} = 20$	$\mathrm{Re} = 40$
Churchill and Bernstein [7]	1.85	2.48	3.38
Li et al. [27]	2.08	2.65	3.47
Wang et al. [38]	–	2.52	–
Present (129×129)	1.84	2.44	3.25
Present (257×257)	1.85	2.46	3.28

and (257×257). A domain with an outer diameter 30 times the cylinder diameter is used. Stretching functions are applied to increase the resolution near the wall surface and in the wake region (cf. Fig. 9). For this test case, classical boundary conditions are imposed: velocity inlet, no-slip condition for the inner cylinder, constant pressure outlet, and the temperature boundaries are a constant temperature for the inner cylinder of $T = 1.0$ and $\partial T/\partial \eta = 0.0$ for the far-field. Provided that the outer boundaries (inlet and outlet) are on one continuous segment, there is a need to handle them based on the azimuthal position. The velocity boundary is used on the left side of the boundary domain, and the pressure boundary is on the right side. The simulation is initialised with a constant temperature of $T = 0.0$.

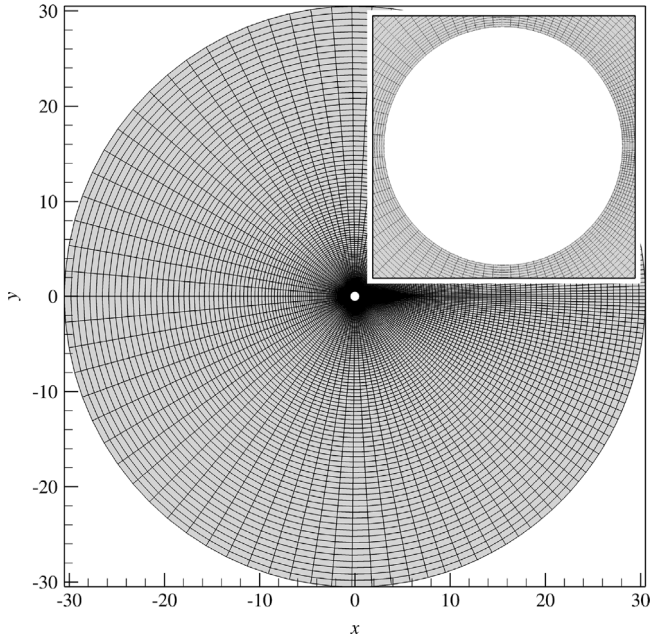

Fig. 9. 2D body-fitted mesh for heated circular cylinder simulations. The overlay, in the upper-right corner, shows the zoomed cylinder surface.

The average Nusselt number of the heated circular cylinder is compared with some of the available literature data in Table 5. For the circular cylinder, the local Nusselt number can be obtained as

$$\mathrm{Nu} = \frac{L_D}{(T_w - T_\infty)} \left(\frac{\partial T}{\partial \eta} \right)_{wall} \tag{40}$$

and the integrated Nusselt number as

$$\overline{\mathrm{Nu}} = \frac{1}{2\pi} \int_0^{2\pi} \mathrm{Nu}\, d\theta, \tag{41}$$

where L_D is the diameter of the cylinder, T_w is the wall temperature and T_∞ is the temperature at the far field.

Table 5 includes the results from Li et al. [27], who have used the GILBM previously developed by He et al. [18] to solve the LBM in domains with irregular geometries. It also includes the results from Churchill and Bernstein [7] who obtained a correlating equation for forced convection in cross-flow on circular cylinders. Ultimately, Table 5 includes Wang et al. [38] as a reference. It can be seen that our results are in agreement with the reference data, and the temperature field can be observed in Fig. 10 for the three steady Reynolds numbers. In addition, the local distribution of Nu over the cylinder surface is examined and compared. Fig. 11 shows that the proposed method agrees well with Ref. [35].

4. Conclusions

In this paper, a generalised thermal LBM is proposed. The fundamental idea is to use a second-order central finite-difference scheme to approximate the lattice Boltzmann equation in curvilinear coordinates for the temperature (passive-scalar) and the velocity distribution functions to simulate thermal flows with body-fitted grids. Typical thermal flows test cases are solved for natural and forced convection with non-Cartesian meshes, namely, natural convection in a square cavity with a stretched mesh, natural convection in a wavy cavity, natural convection in a concentric cylindrical annulus, and forced convection on a heated cylinder. For every test case, the results obtained with the curvilinear LB for thermal simulations agree well with reference data, showing that this simple method can effectively and accurately predict thermal flows with body-fitted boundary conditions.

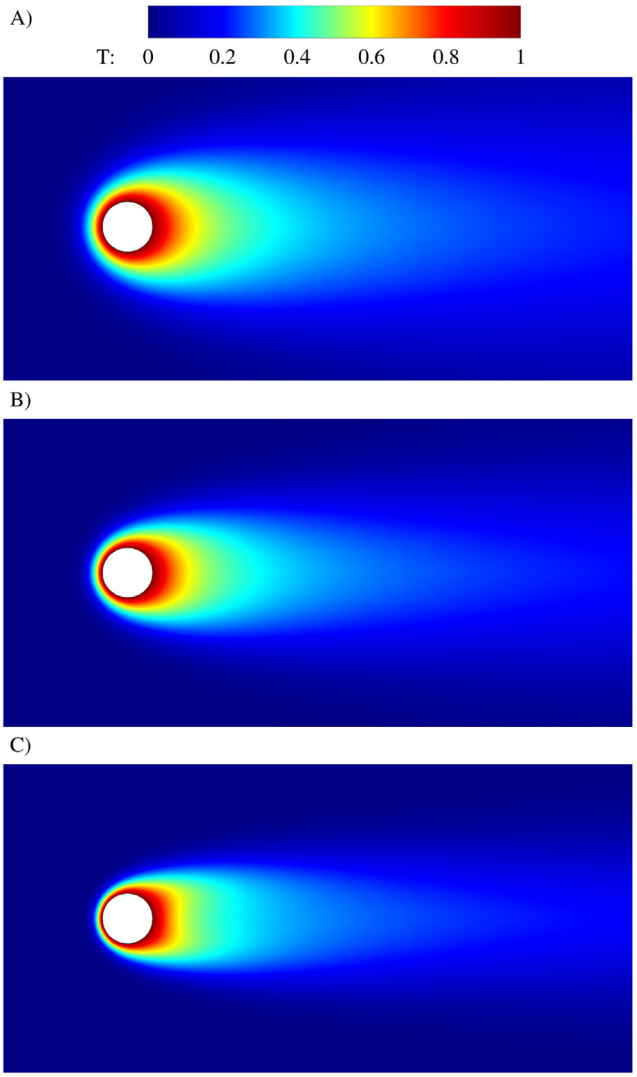

Fig. 10. Temperature field of forced convection on the circular cylinder at different Reynolds numbers: (A) Re = 10, (B) Re = 20 and (C) Re = 40.

Declaration of competing interest

The authors declare that they have no known competing financial interests or personal relationships that could have appeared to influence the work reported in this paper.

Acknowledgements

The authors gratefully acknowledge the support of CONACYT (Consejo Nacional de Ciencia y Tecnología), Mexico and the use of the IRIDIS High Performance Computing Facility, and associated support services at the University of Southampton, in the completion of this work.

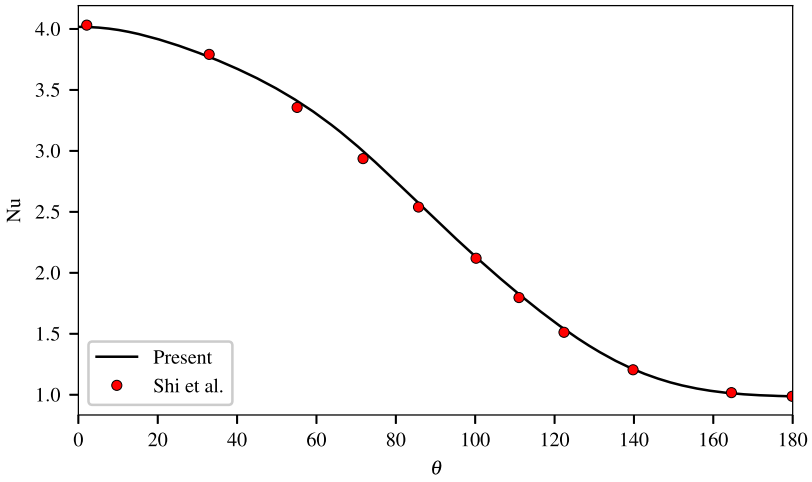

Fig. 11. Nusselt number over the cylinder surface at Re = 20.

References

[1] A.I. Alsabery, T. Tayebi, A.J. Chamkha, I. Hashim, Natural convection of Al_2O_3-water nanofluid in a non-Darcian wavy porous cavity under the local thermal non-equilibrium condition, Sci. Rep. 10 (2020) 18048.
[2] M. Basha, N.A.C. Sidik, Numerical predictions of laminar and turbulent forced convection: Lattice Boltzmann simulations using parallel libraries, Int. J. Heat Mass Transfer 116 (2018) 715–724.
[3] S. Chen, G.D. Doolen, Lattice Boltzmann method for fluid flows, Annu. Rev. Fluid Mech. 30 (1998) 329–364.
[4] H. Chen, O. Filippova, J. Hoch, K. Molvig, R. Shock, C. Teixeira, R. Zhang, Grid refinement in lattice Boltzmann methods based on volumetric formulation, Physica A 362 (2006) 158–167.
[5] Z. Chen, C. Shu, D. Tan, A simplified thermal lattice Boltzmann method without evolution of distribution functions, Int. J. Heat Mass Transfer 105 (2017) 741–757.
[6] C.C. Cho, C.L. Chen, C.K. Chen, Natural convection heat transfer performance in complex-wavy-wall enclosed cavity filled with nanofluid, Int. J. Therm. Sci. 60 (2012) 255–263.
[7] S.W. Churchill, M. Bernstein, A correlating equation for forced convection from gases and liquids to a circular cylinder in crossflow, J. Heat Transfer 99 (1977) 300–306.
[8] L. Crawford, R. Lemlich, Natural convection in horizontal concentric cylindrical annuli, Ind. Eng. Chem. Fund. 1 (1962) 260–264.
[9] G. De Vahl Davis, Natural convection of air in a square cavity: A bench mark numerical solution, Internat. J. Numer. Methods Fluids 3 (1983) 249–264.
[10] R. Deiterding, Block-structured adaptive mesh refinement - theory, implementation and application, ESAIM: Proc. 34 (2011) 97–150.
[11] R. Deiterding, S.L. Wood, Predictive wind turbine simulation with an adaptive lattice Boltzmann method for moving boundaries, J. Phys. Conf. Ser. 753 (2016) 082005.
[12] A. D'Orazio, M. Corcione, G.P. Celata, Application to natural convection enclosed flows of a lattice Boltzmann BGK model coupled with a general purpose thermal boundary condition, Int. J. Therm. Sci. 43 (2004) 575–586.
[13] K. Feldhusen, R. Deiterding, C. Wagner, A dynamically adaptive lattice Boltzmann method for thermal convection problems, Int. J. Appl. Math. Comput. Sci. 26 (2016) 735–747.
[14] M. Grondeau, J.C. Poirier, S. Guillou, M. Y., P. Mercier, E. Poizot, Modelling the wake of a tidal turbine with upstream turbulence, Int. Mar. Energy J. 3 (2020) 83–89.
[15] Z. Guo, C. Shu, Lattice Boltzmann Method and its Applications in Engineering, World Scientific, 2013.
[16] Z.L. Guo, C.G. Zheng, B.C. Shi, Non-equilibrium extrapolation method for velocity and pressure boundary conditions in the lattice Boltzmann method, Chin. Phys. (Overseas Edition) 11 (2002) 366–374.
[17] X. He, S. Chen, G.D. Doolen, A novel thermal model for the lattice Boltzmann method in incompressible limit, J. Comput. Phys. 146 (1998) 282–300.
[18] X. He, L.S. Luo, M. Dembo, Some progress in lattice Boltzmann method. Part I. Nonuniform mesh grids, J. Comput. Phys. 129 (1996) 357–363.
[19] K.A. Hoffmann, S.T. Chiang, Computational Fluid Dynamics -Volume I, Engineering Education System, 2000.
[20] J.T. Holdeman, J.W. Kim, Computation of incompressible thermal flows using Hermite finite elements, Comput. Methods Appl. Mech. Eng. 199 (2010) 3297–3304.
[21] Y. Hu, D. Li, S. Shu, X. Niu, Immersed boundary-lattice Boltzmann simulation of natural convection in a square enclosure with a cylinder covered by porous layer, Int. J. Heat Mass Transfer 92 (2016) 1166–1170.
[22] Y. Hu, X.D. Niu, S. Shu, H. Yuan, M. Li, Natural convection in a concentric annulus: a lattice Boltzmann method study with boundary condition-enforced immersed boundary method, Adv. Appl. Math. Mech. 5 (2013) 321–336.

[23] A.K. Hussein, S.H. Hussain, Heatline visualization of natural convection heat transfer in an inclined wavy cavities filled with nanofluids and subjected to a discrete isoflux heating from its left sidewall, Alex. Eng. J. 55 (2016) 169–186.
[24] C. Kotsalos, J. Latt, B. Chopard, Bridging the computational gap between mesoscopic and continuum modeling of red blood cells for fully resolved blood flow, J. Comput. Phys. 398 (2019) 108905.
[25] T.H. Kuehn, R.J. Goldstein, An experimental and theoretical study of natural convection in the annulus between horizontal concentric cylinders, J. Fluid Mech. 74 (1976) 695–719.
[26] F. Kuznik, J. Vareilles, G. Rusaouen, G. Krauss, A double-population lattice Boltzmann method with non-uniform mesh for the simulation of natural convection in a square cavity, Int. J. Heat Fluid Flow 28 (2007) 862–870.
[27] W. Li, X. Zhou, B. Dong, T. Sun, A thermal LBM model for studying complex flow and heat transfer problems in body-fitted coordinates, Int. J. Therm. Sci. 98 (2015) 266–276.
[28] G. McNamara, B. Alder, Analysis of the lattice Boltzmann treatment of hydrodynamics, Physica A 194 (1993) 218–228.
[29] A.A. Mohamad, A. Kuzmin, A critical evaluation of force term in lattice Boltzmann method, natural convection problem, Int. J. Heat Mass Transfer 53 (2010) 990–996.
[30] Y. Peng, Y.T. Chew, C. Shu, Numerical simulation of natural convection in a concentric annulus between a square outer cylinder and a circular inner cylinder using the Taylor-series-expansion and least-squares-based lattice Boltzmann method, Phys. Rev. E 67 (2003).
[31] U. Projahn, H. Rieger, H. Beer, Numerical analysis of laminar natural convection between concentric and eccentric cylinders, Numer. Heat Transfer 4 (1981) 131–146.
[32] J.A. Reyes Barraza, R. Deiterding, Towards a generalised lattice Boltzmann method for aerodynamic simulations, J. Comput. Sci. 45 (2020) 101182.
[33] X. Shan, Simulation of Rayleigh-Bénard convection using a lattice Boltzmann method, Phys. Rev. E 55 (1997).
[34] M. Sheikholeslami, M. Gorji-Bandpy, G. Domairry, Free convection of nanofluid filled enclosure using lattice Boltzmann method (LBM), Appl. Math. Mech. Volume 34 (2013) 833–846.
[35] J.M. Shi, D. Gerlach, M. Breuer, G. Biswas, F. Durst, Heating effect on steady and unsteady horizontal laminar flow of air past a circular cylinder, Phys. Fluids 16 (2004) 4331–4345.
[36] C. Shu, Application of differential quadrature method to simulate natural convection in a concentric annulus, Internat. J. Numer. Methods Fluids 30 (1999) 977–993.
[37] T. Vijaybabu, S. Dhinakaran, MHD natural convection around a permeable triangular cylinder inside a square enclosure filled with Al_2O_3-H_2O nanofluid: An LBM study, Int. J. Mech. Sci. 153–154 (2019) 500–516.
[38] Y. Wang, C. Shu, C. Teo, Thermal lattice Boltzmann flux solver and its application for simulation of incompressible thermal flows, Comput. Fluids 94 (2014) 98–111.
[39] D. Yu, R. Mei, L.S. Luo, W. Shyy, Viscous flow computations with the method of lattice Boltzmann equation, Prog. Aerosp. Sci. 39 (2003) 329–367.